Contents lists available at ScienceDirect

# Biomaterials

journal homepage: www.elsevier.com/locate/biomaterials

# Superparamagnetic iron oxide nanoparticle-embedded encapsulated microbubbles as dual contrast agents of magnetic resonance and ultrasound imaging

Fang Yang [a], Yixin Li [a], Zhongping Chen [a], Yu Zhang [a], Junru Wu [b], Ning Gu [a],*

[a] Jiangsu Laboratory for Biomaterials and Devices, State Key Laboratory of Bioelectronics, School of Biological Science and Medical Engineering, Southeast University, Nanjing 210096, China
[b] Department of Physics, University of Vermont, Burlington, VT 05405, USA

A B S T R A C T

An encapsulated microbubble (EMB) of a novel construct is proposed to enhance the magnetic resonance imaging contrast by introducing superparamagnetic iron oxide (SPIO) nanoparticles (mean diameter is 12 nm) into the polymer shell of the microbubble. Such microbubble vesicle has nitrogen gas in the core and its mean diameter is 3.98 μm. An *in vitro* MR susceptibility experiment using a phantom consisting EMBs has shown that the relationship between the transverse relaxation rate $R_2$ and the $Fe_3O_4$ nanoparticle concentration in the shell (the volume fraction of EMBs is kept constant) can be fitted to a linear function and an exponentially growth function is observed between $R_2$ and the SPIO-inclusion microbubble concentration. The *in vivo* MRI experiments also show that the SPIO-inclusion microbubbles have longer contrast-enhancement duration time in rat liver than non-SPIO-inclusion microbubbles. An *in vitro* ultrasound imaging experiment of SPIO-inclusion microbubbles also shows that they can enhance the ultrasound contrast significantly. Additionally, the interaction between the SPIO-inclusion microbubbles and cells indicates that such microbubble construct can retain the acoustic property under the ultrasound exposure by controlling the SPIO concentration in the shell. Therefore, the proposed SPIO nanoparticle-embedded EMBs potentially can become effective MR susceptibility contrast agents while also can be good US contrast agents.

© 2009 Elsevier Ltd. All rights reserved.

## 1. Introduction

When a small magnetic object is introduced into a medium exposed to a uniform static external magnetic field along $z$ direction, $B_z$, the locally arisen perturbation to the magnetic field is related to the object's geometry, dimension and magnetic susceptibility [1]. For a spherical particle located at the origin of the spherical coordinates, the magnetic-field perturbation $\delta B_z$ at the position $(r, \theta)$ is described by Eq. (1) in SI units [1,2]:

$$\delta B_z(r, \theta) = (1/3)B_z \Delta\chi(R/r)^3 \left(3\ \cos^2\theta - 1\right) \qquad (1)$$

where $R$ is the radius of the particle, $\Delta\chi$ is the magnetic susceptibility difference between the object and the medium. The perturbation is short-ranged as $1/r^3$ and positive when $0° \leq \theta \leq 54.7°$ and $125.3° \leq \theta \leq 180°$ (it reaches the maximum at $\theta = 0°$ and $180°$), and

is negative in other region of $\theta$. The contrast enhancement in magnetic resonance imaging (MRI) by the presence of the magnetic particle is the result of the above-described local non-uniformity of the magnetic fields, which leads to a rapid dephasing of protons and shortens the spin–spin relaxation time ($T_2$) and increases the transverse relaxation rate ($R_2$).

Encapsulated microbubbles (EMBs) consisting of a specific gas surrounded by a polymer shell are commonly used as contrast agents to enhance contrast in ultrasound (US) imaging because their acoustic impedances are significantly different from that of the surrounding tissue or fluid [3,4]. It has been shown [5,6] that EMBs excited by the moderate ultrasound (the negative peak acoustic pressure $P < 0.25$ MPa) can transiently increase permeability of membranes of cells letting DNA, antibodies, or anticancer drugs in a solution entering the cells; this technique is called sonoporation. It has been further shown that EMBs can also be used as contrast agents in MRI [7]. The rationale is that the presence of an EMB in tissue introduces the magnetic susceptibility difference $\Delta\chi$ at the gas–tissue interface; the contrast is particularly evident when $B_z$ is strong and the core gas is paramagnetic [8]. Ueguchi

et al. [9] have used EMBs in a phantom experiment and showed that they were useful as MRI contrast agents when $B_z$ was 1.5 T or greater. Other known applications of EMBs include functional lung MR imaging [10] and intra-cardiac pressure sensing for noninvasive manometry associated with MRI [11].

For a given EMB concentration, $R_2$ is known to be linear to $B_z$ [1]. Although it has been shown that EMBs can be used as MRI contrast agent in $B_z$ as low as 1.5 T, significant contrast enhancement can only be achieved *in vivo* by using much higher $B_z$ [9]. Various techniques have been adopted to break this limitation [7–9,12]. A practical and convenient way, in our opinion, is to embed para-magnetic iron oxide, or other magnetic materials into the shell of an EMB to increase the MR susceptibility. To minimize the possible distortion to the overall quality of the MRI image, magnetic materials introduced into the shell should be small while still obtain high susceptibility [1]. Since it is known that superparamagnetic iron oxide (SPIO) nanoparticles can enhance $T_2$-weighted MRI images [13–15], they can be ideal candidates to be embedded into EMBs' shell for MRI contrast agents.

Ultrasound is a real-time, non-ionizing, cost effective, and widely available imaging modality, but it has poor tissue discrimination ability [16,17]. MR imaging is also a noninvasive imaging tool with exquisite soft tissue contrast and multi-planar imaging capacities, but it cannot provide real-time images and usually it has a relatively long imaging time [18]. In many clinical applications, US and MRI are complimentary; both modalities are usually needed to discern possible pathological changes in tissue. If the dual-modality contrast agents combining the advantages of the US and MR imaging can be applied clinically, adequate and comprehensive imaging information can be obtained [19–21] by just using one kind of contrast agents. It is not only convenient to medical professionals but also reduces the health-care cost. In this work, we have prepared a special microbubble construct which is loaded with both gas and superparamagnetic iron oxide ($Fe_3O_4$) nanoparticles. The $Fe_3O_4$ SPIO particles have susceptibility as high as 70 (in comparison, tissue in general is weakly diamagnetic and its susceptibility is in the range: $-11.0 \times 10^{-6} < \chi_{tissue} < -7.0 \times 10^{-6}$) [1]. This construct using nanometer size particles can effectively emulate the desired large susceptibility difference between EMBs and their surrounding medium. Thus, such EMBs can potentially serve as effective MRI contrast agents.

First, we present briefly the preparation method as well as the main physical characterization features of the SPIO $Fe_3O_4$ nano-particle-inclusion EMBs. To measure their characteristics as MR contrast agents *in vitro* and *in vivo*, a 7 T MR scanner was used with the scanner sequence of $T_2$ (spin–spin interaction time constant)-weighted fast spin-echo. We identified that transverse relaxation rate, $R_2$, for the SPIO nanoparticle-inclusion EMBs increases expo-nentially when the EMBs' volume fraction increases, which is different from the linear relation of the transverse relaxation rate, $R_2$, *vs* the EMB volume fraction for non-SPIO-inclusion EMBs. The possible different physical mechanisms of transverse relaxivity enhancement for SPIO-inclusion EMBs and non-SPIO-inclusion EMBs were explored. Further, the longer contrast-enhancement duration time of SPIO-inclusion EMBs was found in rat liver MRI experiments, which was quantified by the signal-to-noise ratio (SNR) of the acquired MR images.

In addition to their MRI properties, the ultrasound contrast-enhancement experiment and the interaction between the cells and SPIO-inclusion EMBs under US exposure were also studied. We have shown the newly designed EMBs can oscillate vigorously under a moderate acoustic field (the negative peak acoustic pres-sure $P < 0.25$ MPa). The $Fe_3O_4$ nanoparticles can be delivered *via* a transient sonoporation process into the cells through the cell membranes [22,23]. The cell experiments indicate that the EMBs

with appropriate concentration of SPIO $Fe_3O_4$ nanoparticles encapsulated in the shell retain the highly echogenic and disten-sible properties, which can make the SPIO-inclusion EMBs not only serve as ultrasound contrast agents [24], but also as the effective MR imaging contrast agents.

## 2. Materials and methods

### 2.1. Fabrication of EMBs

Microbubbles with polyvinyl alcohol (PVA) outer layer and a poly(DL-lactide) (PLA) inner layer were prepared using a double emulsion solvent evaporation interfacial deposition (water-in-oil-in-water emulsion) process. It was reported that both PVA and PLA have good biocompatibility and biodegradability [25,26]. An organic solution (10.00 ml) was prepared containing PLA (0.50 g, purchased from the Shandong Key Laboratory of Medical Polymer Materials, China) and hydrophobic SPIO $Fe_3O_4$ nanoparticles [27] (mean diameter = 12 nm, Jiangsu Laboratory for Biomaterials and Devices) in methylene chloride at 25 °C. The amount of added SPIO nanoparticles was varied. EMBs with different SPIO-inclusion amounts were prepared. To generate first SPIO-inclusion bubble emulsion, Milli-Q water (1.00 ml) and Span 80 (0.50 ml) were added to the organic solution and continuously soni-cated at 100 W with a probe while constant purging using a steady (4 ml/min) stream of $N_2$ gas for 5 min. The free SPIO nanoparticles were separated by using the magnetic isolation method [28]. The first bubble emulsion was then poured into a 5% PVA (w/v, from Alfa Aesar®) solution including Tween 80 (0.5 ml) and mixed mechanically for 2 h to form stable double-layered emulsion bubbles without the residual organic solvent. After reaction, the final emulsion became milk-white. The microbubble solution was then transferred to a custom made centrifuge tube to isolate different size microbubbles by using the differential centrifugation methods [29]. The collected agent was stored at 4 °C in tightly capped vials sealed with paraffin films for experimental analysis. Before the sample was used, it was diluted to the concentration of $7$–$8 \times 10^8$ microbubbles/ml in a phosphate buffer solution (PBS, pH = $7.4 \pm 0.1$). The EMBs without SPIO inclusion was prepared by the same way just without adding the SPIO $Fe_3O_4$ nanoparticles in the methylene chloride. Fig. 1 is the schematic diagram illustrating the designed SPIO-embedded EMB structure.

### 2.2. The characterization of EMBs

The mean diameter size and size distribution of EMBs were analyzed using a Laser Diffraction Particle Size Analyzer (Mastersizer 2000, England). The concen-tration of EMBs was measured by a hemocytometer. The concentration of $Fe_3O_4$ nanoparticles embedded in the shell of EMBs was determined by an Atomic Absorption Spectrometer (180-80 Hitachi, Japan) [30].

The morphology of nanoparticle-embedded EMBs was studied using a trans-mission electron microscope (H800-3 Hitachi, Japan) operating at 100–175 kV accelerating voltage. Samples were fixed in 1% $OsO_4$ for 1 h, dehydrated in acetone and then embedded in liquid epoxy resin. After hardening, the resin blocks were sectioned in 50 nm sections and stained in uranyl acetate and lead citrate before photographed.
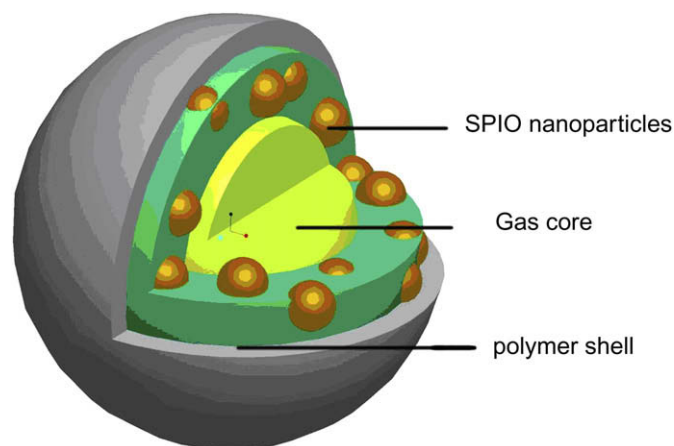


**Fig. 1.** The schematic diagram of the designed SPIO-inclusion EMB. The structure of an EMB can be briefly described as follows: the core gas of the first emulsion microbubble was $N_2$, encapsulated by a shell of poly-D,L-lactide (PLA). Hydrophobic SPIO nano-particles were distributed in the PLA layer during the formation of the first bubble emulsion. The second shell was poly(vinyl alcohol), PVA, solution.

The magnetization property at the room temperature (20 °C) of the SPIO-inclusion microbubbles was further studied by using a vibrating sample magnetometer (VSM, Model 7407, Lake Shore Cryotronics, Inc., OH, USA). The samples studied include the microbubbles with different SPIO-inclusion concentration microbubbles and the non-SPIO-inclusion microbubbles. All the tested samples were measured under the suspension solution condition. Due to the extremely low magnetic moment of the samples, the correct hysteresis loops were obtained after subtracting the off-set background signals using the procedure suggested by the manufacturer's instructor's manual. Saturation magnetization, coercive force and remnant magnetization were obtained from the hysteresis loops. Each sample was measured in triplicate.

### 2.3. In vitro MRI experiments

An EMB phantom study was performed using a 7.0 Tesla Micro-MRI (PhamaScan, Bruker, Germany). The sample was placed in an Eppendorf tube of 1 cm in diameter. At the beginning of each measurement, automatic shimming and preparation scan were performed with the de-ionized water. The imaging parameters for $T_2$ (spin–spin interaction relaxation time constant)-weighted fast spin-echo were set as repetition time (TR) = 4000 ms, echo time (TE) = 108 ms, number of excitations (NEX) = 1, echo train length = 16. Images were obtained with a matrix size of $256 \times 256$, section thickness of 2 mm and field of view (FOV) of 10 mm × 10 mm. Then we continuously measured the resulting change in the transverse relaxation time ($T_2$) of the microbubble suspension by recording the above mentioned single-slice gradient-echo signal. No phase or frequency encoding was used. According to the mono-exponential signal decay as function of TE, the transverse relaxation time ($T_2$) of well-mixed microbubble suspension can be estimated.

### 2.4. Measurement of $T_2$ of SPIO-inclusion and non-SPIO-inclusion microbubbles

There are three types of EMBs, including SPIO-inclusion EMBs (86.47 µg/ml SPIO concentration), non-SPIO-inclusion EMBs, and non-SPIO-inclusion EMBs mixed with SPIO particles of the same concentration, were studied. The concentration of the samples was $7–8 \times 10^8$ microbubbles/ml. Then they were diluted to different volume fractions from 100% to 1% by the addition of PBS (pH = 7.4 ± 0.1). One milliliter Eppendorf tubes filled with EMBs in the PBS (pH = 7.4 ± 0.1) solution were served as phantoms. The test tube containing EMB solution was continuously rotated by hand gently to ensure uniformity of EMB suspension in the test tube prior to MR measurement and then was placed in the scanner vertically. Immediately after that, the imaging sequence started to avoid the EMBs migrating upward to the top due to the buoyant force. The transverse relaxation rate ($R_2$) as a function of bubble volume fraction was then calculated based on the measured $T_2$ data.

Furthermore, in order to find the optimum embedded SPIO $Fe_3O_4$ nanoparticle amount in the shell, the microbubbles with different SPIO-inclusion amounts (0, 5.73, 12.06, 33.14, 54.23, 86.47, 105.69, 122.85, 145.24, 180.23 µg/ml) were prepared. All $T_2$ were measured under the concentration of $7–8 \times 10^8$ EMBs/ml to calculate the transverse relaxation rate ($R_2$) as a function of iron oxide amount.

### 2.5. In vitro ultrasound imaging experiment

A de-gassed water tank 10 cm deep, 15 cm long, 7 cm wide was used in the in vitro experiment and 1 cm thick sponge layer was stick to the bottom as the acoustic absorber. The sample was injected into a latex bag and then the bag was sealed and fixed in the water tank with a distance of 6 cm from the bottom of the tank. The ultrasonic imaging system of GE LOGIQ9 scanner with a 3.5 MHz ultrasound
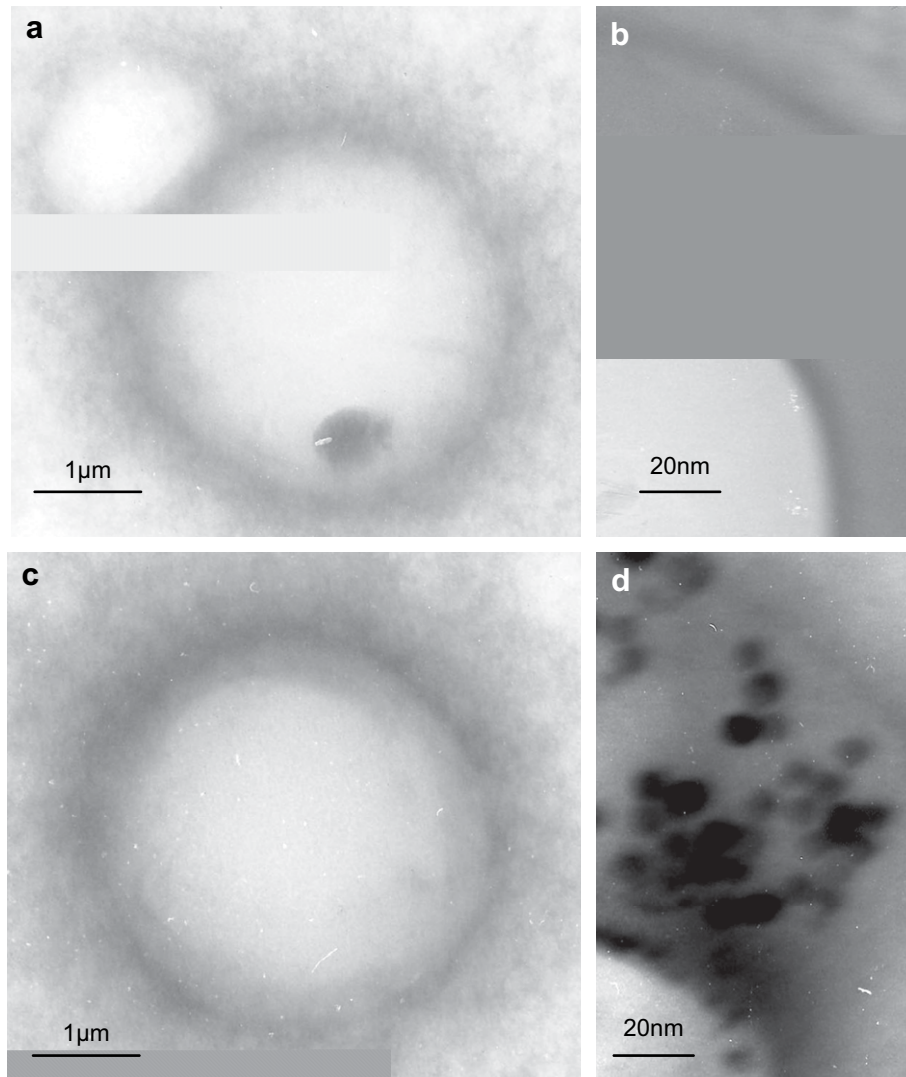


**Fig. 2.** (a) A TEM image of the microbubbles without SPIO inclusion; (b) A TEM image of an SPIO-inclusion microbubble; and (c) and (d) are the enlarged views of a portion of the shell shown in (a) and (c). It can be observed that the nanoparticles are distributed in the shell.

transducer was used as a transmitter as well as a receiver. All images were acquired with the same instrument parameters (Mechanical Index (MI) = 0.1; gain = 10 dB). Every sample was scanned 3 times.

To quantitatively measure the brightness of the ultrasound imaging of different SPIO-inclusion microbubbles, a 'mean grey scale' was calculated as the average of the grey scale levels of all pixels within a region of interest (ROI). The image sampled by the imaging system was 8-bit; thus the range of pixel grey scale level was 0–255. To reduce potential bias in performing ROI selection, a MATLAB computer program (The Math Works, Inc., Natick, MA) was developed to automatically define the ROIs at the fixed positions for all images, and the mean grey scale for each ROI was calculated separately in this program. For every sample, the images of the three scanned segments processed, and then the average value of the three ROIs' mean grey scale was adopted as the mean grey scale of the sample.

### 2.6. Microbubble interaction with tumor cells under ultrasound exposure

In order to investigate the effectiveness of SPIO-inclusion EMBs acoustically, the possible sonoporation effects induced by the interaction between EMBs and SMMC-7721 liver tumor cells was investigated under the moderate US exposure.

SMMC-7721 cells, a human liver carcinoma cell line, were purchased from Cell Bank of Type Culture Collection of Chinese Academy of Sciences (Shanghai, China). They were cultured as mono-layers in RPMI 1640 medium supplemented with 10% fetal bovine serum (FBS), and incubated at 37 °C with 5% $CO_2$ in a humidified air atmosphere. Exponentially growing cells were harvested and resuspended in fresh RPMI 1640 media with 10% FBS. Before mixing with EMBs, the suspended cell solution was separated using a centrifuge at 1000 rpm for 8 min and resuspended in the fresh PBS (pH = 7.4 ± 0.1). The concentration of the cells was diluted to a concentration of about $7–8 \times 10^8$ cells/ml with the same concentrations of the EMB solution. Mixed solution of cell (1 ml) suspension and EMBs (0.5 ml) was introduced in a 10 ml plastic test tube with 15 mm diameter and 75 mm length capped by a rubber stopper (US was propagating upwards from the bottom of the test tube, a rubber stopper was used as an sound absorber to minimize a standing-wave effect; there was no air between the cap and suspension). The US exposure of the sample in a test tube was achieved in a water tank filled with de-gassed and de-ionized water. The detailed description may be referred to our previous work [31]. Briefly, an arbitrary waveform generator (Agilent 33250A, USA) was used to produce a sinusoidal radio frequency signal; it contained repeated 1 MHz tone-bursts, 20 cycles per tone-burst at a pulse-repetition-frequency (PRF) of 10 kHz. It was then amplified by a 50 dB broadband RF power amplifier (ENI 2100 L, Rochester, NY, USA), and used to drive a focusing transducer of radius 9.2 cm. The central frequency of the transducer is 1 MHz and the focal distance was 8 cm. The acoustic field was measured using a needle pvdf broadband piezoelectric hydrophone (NP1000, NTR Systems, Seattle, WA) with an active sensing diameter of 0.2 mm. The sample test tube was positioned in the water tank by clamping the top end of the sample tube on a small steel fixture at a location that positioned the sample tube along the axial and radial center of the transducer. At the same time, the sample tube was rotated at 60 rpm by a DC motor throughout the exposure period to mix EMBs with cells evenly. The in situ spatial peak negative pressure amplitude after the attenuation correction, P, changed with the applied voltage to the power amplifier and calibrated by a needle broadband hydrophone for the cases discussed in the Results section, its value was 0.25 MPa unless specified otherwise. The total exposure time was 40 s.

### 2.7. Microbubble MR susceptibility contrast imaging of rat liver

Fifteen normal adult rats (200–250 g) were used in this study. All in vivo studies were performed according to a protocol approved by the Internal Review Board and by the animal care committee of the Southeast University. They were selected and randomized into three groups (5 rats every group). One group was injected SPIO inclusion (86.47 μg/ml) bubbles. Another group was injected the bubbles without SPIO inclusion. The third control animal group was performed to rule out the possibility of enhancement caused by the sterile saline. The rats were anesthetized with isoflurane (1.5% vol. at 2 L/min) via a nose cone. Body temperature was maintained at 37 °C. The agents had a final concentration of $7–8 \times 10^8$ micro-bubbles/ml. For each single injection, a syringe with 23 gauge needles was used to draw the bubble solution according to each rat's body weight (0.4 ml microbubbles/kg body weight). The suspension was then injected through tail vein of rats. Immediately after administration, the injection port was flushed with 1 ml of saline solution.

The in vivo liver MRI experiment was performed on rats with the use of a 10 cm circular surface coil in transmit/receive mode conducting on 7 Tesla Micro-MRI (PharmaScan, Brukers, Germany). The magnet was equipped with gradient coil and ParaVision 4.0 acquisition/processing software. Each rat was fixed in a prone position with its abdomen resting on bottom of the coil. Dynamic susceptibility imaging was performed with $T_2$ 2D fast low-angle shot (FLASH) sequence with the respiratory gating control. The parameters were TR/TE = 100 ms/8 ms, flip angle = 350°, FOV = 10 mm × 10 mm, slice thickness = 2 mm, NEX = 2, in-plane resolution = $0.78 \times 0.78$ mm$^2$, and temporal resolution = 21 s. Anatomical images were acquired under similar protocol, except that TE = 4 ms. The total imaging observation time was 2 h for each rat.

## 3. Results and discussion

### 3.1. Characterization of SPIO-inclusion EMBs

The $Fe_3O_4$ nanoparticle-inclusion EMBs were harvested from the solution using differential centrifuge separation method. After separation, the size distribution of SPIO-inclusion EMBs of various concentrations of $Fe_3O_4$ nanoparticles embedded in the shell of EMBs was measured. A major peak of the size distribution of SPIO-inclusion microbubbles at the diameter of 3.98 μm with poly-disperity index (PI, an indication to define the size distribution broadness of the microbubbles sample) of 0.874 was collected. The mean diameter of non-SPIO-inclusion microbubbles was 3.98 μm with PI of 0.425. This result suggests that the addition of SPIO in the polymer shell does not significantly affect EMB size distribution. The concentrations of SPIO encapsulated in the shell were 0, 5.73, 12.06, 33.14, 54.23, 86.47, 105.69, 122.85, 145.24, 180.23 μg/ml respectively. Under the concentration of $7 \times 10^8$ EMBs/ml, the SPIO concentration in one microbubble was 0, $0.82 \times 10^{-8}$, $1.72 \times 10^{-8}$, $4.73 \times 10^{-8}$, $7.75 \times 10^{-8}$, $12.35 \times 10^{-8}$, $15.10 \times 10^{-8}$, $17.55 \times 10^{-8}$, $20.75 \times 10^{-8}$, $25.75 \times 10^{-8}$ μg/EMB accordingly.

Fig. 2 includes TEM images of the EMBs. The one on the top-left (Fig. 2a) is from an EMB with the polymer shell; the interface between the shell and gas can be discerned (Fig. 2b). The one on the bottom-left (Fig. 2c) is a SPIO-inclusion EMB TEM image. That the hydrophobic SPIO $Fe_3O_4$ nanoparticles are dispersed in the shell of the bubbles randomly (somewhat clustered) are seen in Fig. 2d (a magnified portion of the shell shown). The evaluated thickness of the shell ranges from 50 nm to 70 nm. Fig. 3 shows the magnetization property of the SPIO-inclusion microbubbles. The magnetic measurement of SPIO for microbubble inclusion indicates superparamagnetic behavior at room temperature with no hysteresis and perfect Langevin behavior [27]. After the SPIO is encapsulated in the shell of mcirobubbles, there is also no remnant magnetization observed in the VSM curve, which indicates that the inclusion material has been preserved super-paramagnetic characteristics. With the increase of SPIO-inclusion concentration in the shell of microbubbles, the saturation
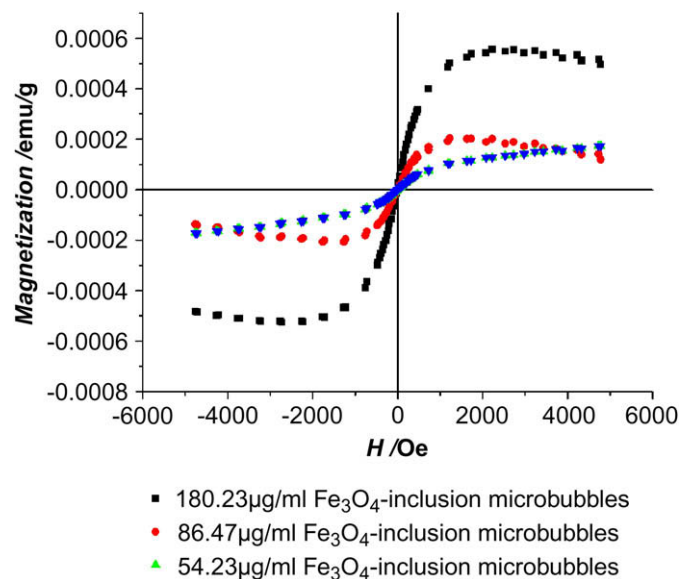


**Fig. 3.** VSM curve of microbubbles with different concentrations SPIO inclusion. According to these hysteresis loops, the saturation magnetization, coercive force and remnant magnetization can be obtained.
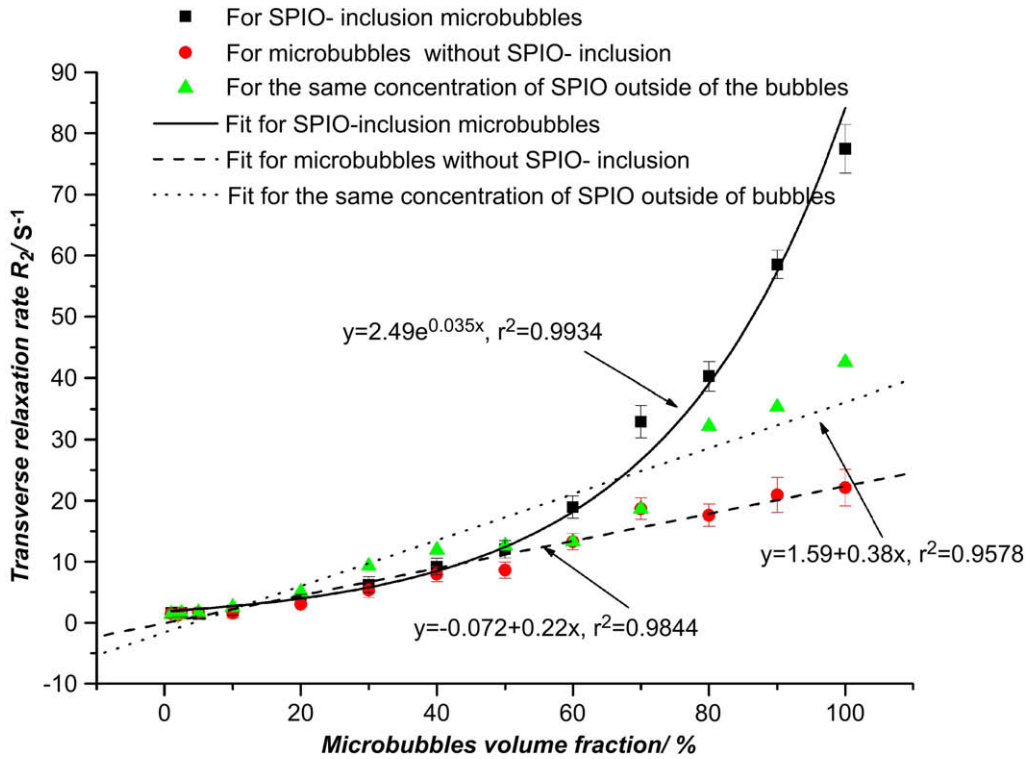
**Fig. 4.** The relationship between the transverse relaxation rate (R$_2$) and the volume fraction of three types of microbubbles: (1) SPIO nanoparticle-inclusion microbubbles, (2) microbubbles without SPIO inclusion and (3) bubbles with the same concentration of SPIO particles existing in a solution outside of the microbubbles.

magnetization is also increased. As a control, we have found that the VSM curve cannot be obtained in the microbubbles without SPIO inclusion.

The sonication and emulsion–evaporation preparation methods are commonly used methods for preparing polymer coated microbubbles. However, the size distribution of microbubbles obtained is inevitably relatively broad. For MR susceptibility applications where microbubble size is also critical, the differential centrifugation is used to obtain different size distribution microbubbles [29]. We have chosen to evaluate 3.98 ± 1.7 μm microbubbles as MRI contrast agents to study.

### 3.2. Contributions to transverse relaxation rate by three types of EMBs

Fig. 4 shows the dependency of R$_2$ on EMB volume fraction of a phantom for three different samples: (1) SPIO-inclusion EMB suspension; (2) Non-SPIO-inclusion EMB suspension; (3) Non-SPIO-inclusion EMB suspension mixed with SPIO particles of the same concentration. An approximately linear relationship was observed for both (2) and (3). The linear relationship was predicted in a theoretical study of the EMBs' susceptibility effect conducted by Dharmakumar et al. [11] and was also observed in an earlier EMB
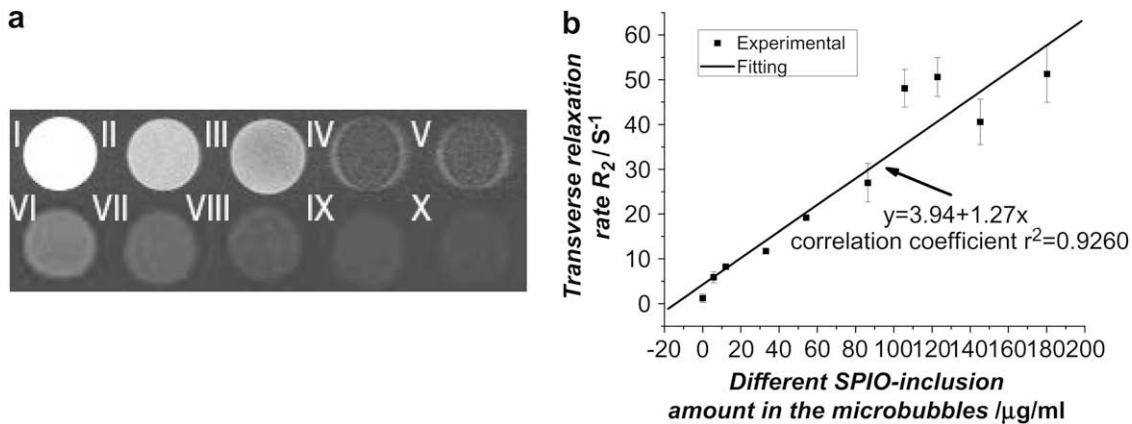


**Fig. 5.** The *In vitro* MRI images using 7 T scanner is indicated in the Fig. 4(a). I: de-ionized water, II: EMBs without SPIO inclusion, SPIO-inclusion EMBs with different SPIO concentrations (III–X are 5.73, 12.06, 33.14, 54.23, 86.47, 105.69, 122.85, 145.24, 180.23 μg/ml respectively). After the corresponding T$_2$ computed from the T$_2$-maps were obtained. The relationship of R$_2$ *vs* SPIO inclusion (μg/ml) is shown in (b). The linear fit was obtained between the SPIO-inclusion concentration in the microbubbles and the transverse relaxation rate (R$_2$). From this curve, it is found that the effect of increasing total magnetic nanoparticle density in the shell is related to increasing the susceptibility effects of the microbubbles.
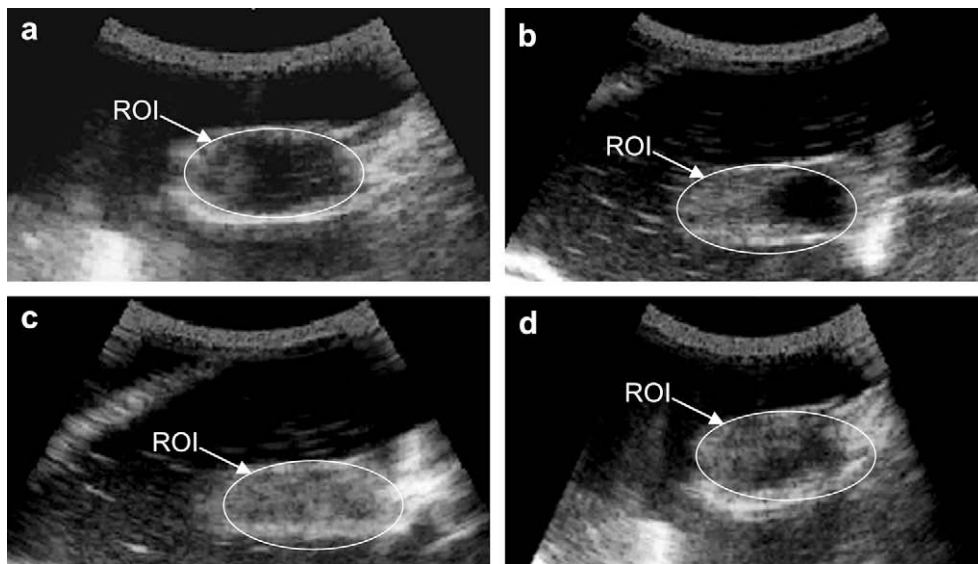
**Fig. 6.** The *in vitro* ultrasound imaging in the different samples (a) de-gassed and de-ionized water; (b) the non-SPIO-inclusion microbubbles; (c) and (d) are 86.47 µg/ml and 180.23 µg/ml SPIO concentration inclusion microbubbles respectively.

phantom study [9]. We have further found for SPIO-inclusion EMBs the growth of $R_2$ increases much faster when EMB volume fraction increases. The data fitted an exponential curve very well with the square of the correlation coefficient $r^2 = 0.9934$. The high concentration (greater than 60%) SPIO-inclusion EMB solution can enhance transverse relaxivity significantly.

In the *in vitro* MR phantom experiment, the measured transverse relaxation rate ($R_2$) of the samples may be described by Eq. (2):

$$R_2^{Total} \approx R_2^{Bubble} + R_2^{SPIO} \tag{2}$$

The overall transverse relaxation rate $R_2^{Total}$ is considered as the sum of that contributed by EMBs, $R_2^{Bubble}$, and that contributed by SPIO particles, $R_2^{SPIO}$. Generally speaking, $R_2^{SPIO} \gg R_2^{Bubble}$. From Fig. 4, we observed that $R_2^{SPIO}$ contributed by SPIO $Fe_3O_4$ nanoparticles embedded in EMBs is greater than that contributed by the free SPIO $Fe_3O_4$ nanoparticles in the solution of the same concentration when volume fraction is greater than 60%. A possible explanation may come from the fact that with the same mass concentration of SPIO $Fe_3O_4$ nanoparticles (µg/ml) in a suspension, EMBs' role to hold the nanoparticles in the shells made numbers of SPIO localized and concentrated per volume inside the shell, thus the number of SPIO per volume much higher than those anywhere for the free SPIO case. Since in this case the effect due to highly concentrated SPIO dominates, the linear relationship condition with respect to $\Delta\chi$ (Eq. (1)) based on the uniformly distributed EMBs' susceptibility effect is no longer valid. In fact, the effect by adding the number of SPIO per volume becomes quite nonlinear.

### 3.3. Different SPIO number concentrations of EMBs vs $R_2$

Following the study above, the relation how the transverse relaxation rate changes with the number concentration of SPIO nanoparticles in the shell of SPIO-inclusion EMBs was explored. Theoretical prediction [11] indicates that non-SPIO-EMBs suspension is linearly proportional to the number density of EMBs. Fig. 5(a) includes MRI images of various cases, including de-ionized water, EMBs without SPIO-inclusion, SPIO-inclusion EMBs with different SPIO concentrations (5.73, 12.06, 33.14, 54.23, 86.47, 105.69, 122.85, 145.24, 180.23 µg/ml respectively). They also

suggest that the more concentration of SPIO in EMBs gives the best contrast of MRI image to change the $T_2$ signal. Fig. 5(b) is experimental results of $R_2$ *vs* SPIO inclusion (µg/ml). The data fitted to a linear function nicely with $r^2 = 0.9260$. It suggests that the linear relationship prediction holds well even with the SPIO-inclusion EMBs.

### 3.4. In vitro ultrasound contrast enhancement

The ultrasound images of the de-gassed and de-ionized water, the non-SPIO-inclusion microbubbles and different SPIO concentration inclusion microbubbles were captured; they are shown in Fig. 6a–d respectively. Compared with Fig. 6a of the de-gassed and de-ionized water, the brighter area can be seen distinctly in the SPIO-inclusion microbubbles. The different types of microbubbles have different brightness. The change curve of the mean grey scales within the ROIs of the different SPIO concentration inclusions are
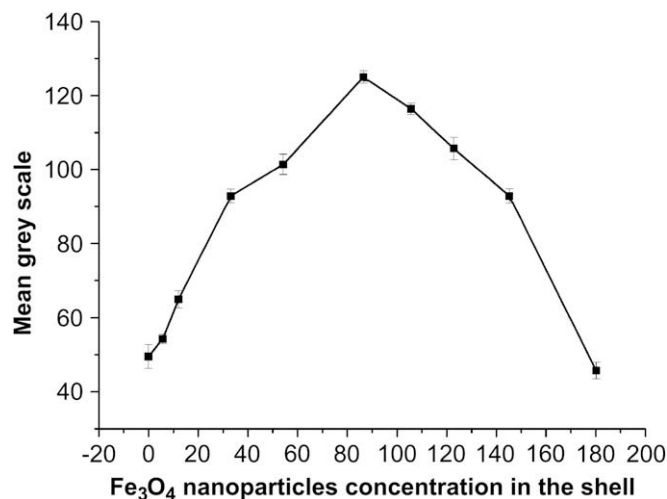


**Fig. 7.** The ultrasound contrast-enhancement change curve of different SPIO concentrations in the shell. With the increase of the inclusion concentration, the mean grey scale of ultrasound imaging increased at first and then decreased.
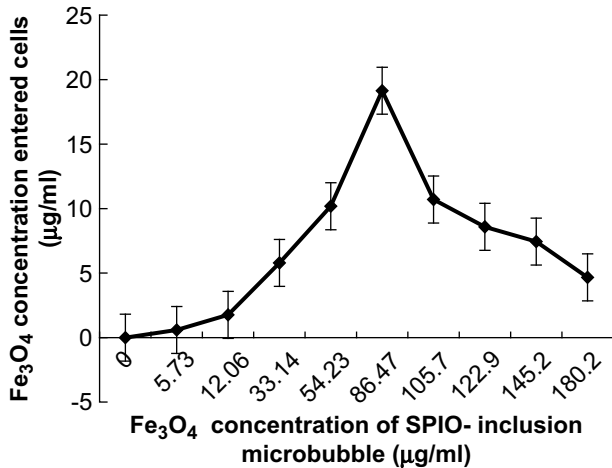
**Fig. 8.** $Fe_3O_4$ nanoparticle concentration deposition into the tumor cells by the SPIO-inclusion microbubbles under the ultrasound exposure. The applied ultrasound was 0.25 MPa acoustic pressure amplitude and exposure time was 40 s. The peak delivery efficiency of the $Fe_3O_4$ nanoparticles into the cells illustrates that there is an optimum nanoparticle concentration that can be embedded into the shell of an EMB while the EMB can still maintain effective acoustic property under US exposure.

shown in Fig. 7. This curve indicates that with the increase of the inclusion concentration, the ultrasound contrast enhancement is increased till the insertion concentration reaches about 86.47 µg/ml. When the inclusion concentration exceeds 86.47 µg/ml, the enhancement efficiency of ultrasound contrast becomes a little poorer.

### 3.5. Deposition of nanoparticles in the tumor cells of different SPIO-inclusion EMBs under ultrasound exposure

The sample of SPIO-inclusion EMBs and cell mixture was soni-cated using the described parameters. Rapidly after the sonication, the cells were isolated and washed by the centrifugation flotation method. The concentration of $Fe_3O_4$ nanoparticles entered the SMMC-7721 cells *via* sonoporation which was measured by the atomic absorption spectrometric technique. Fig. 8 shows the concentration of $Fe_3O_4$ nanoparticles that entered cells *vs* $Fe_3O_4$ nanoparticle concentration embedded into the shell. Each data point represents the average of triplicate measurements and the error bars are the standard deviations (SDs) of the triplicate measurements. The curve of Fig. 8 indicates that with the increase

of $Fe_3O_4$ nanoparticles embedded into the shell, the concentration of nanoparticles entering the cells increased at first and then decreased. This two-stage phenomenon suggests: (1) at the beginning, when the embedded nanoparticle number was small, the mechanical property of EMBs did not change significantly, therefore their interaction with cells did not change much. Thus the nanoparticle entered into cells was an increasing function of the embedded $Fe_3O_4$ number. When the number of $Fe_3O_4$ became greater enough, the trend was reversed because the EMB became too stiff and less effective to interact with cells. It concludes that the embedded nanoparticles in the shell can influence the mechanical properties of EMBs in the ultrasound field. Too many SPIO nano-particles embedded into EMBs could make them stiffer and acoustically less effective under ultrasound exposure. Results shown in Fig. 8 suggest that the optimum concentration of SPIO in EMBs to keep the acoustic viability of EMBs is near 86.47 µg/ml. The US imaging application of the SPIO-embedded EMBs using an ultrasonic imaging system has already been reported in our previous paper [24].

### 3.6. In vivo rat liver MRI

Microbubble susceptibility contrast enhancement was consis-tently observed in the fifteen rats studied. Fig. 9 illustrates the typical MRI anatomical images after injection of SPIO-inclusion microbubbles. Fig. 9(a) is the image pre-injection, and Fig. 9(b)–(e) shows the postcontrast images about 10 min, 30 min, 60 min, 70 min, 80 min, 100 min and 120 min. It can be seen that the overall signal in the liver region was negatively enhanced after injection of the microbubble contrast agents.

Typical SNR time-course of the $T_2$-weighted images in a rat liver during microbubble injection is shown in Fig. 10. The measurement ROIs is selected from a relatively homogeneous four regions of liver tissue region according to the first image of Fig. 9. Although the $T_2$ signal negative enhancement of MRI immediately starts to appear when the two types of microbubbles are injected, the SNR time-course of SPIO-inclusion microbubbles has longer negative enhancement than microbubble non-SPIO inclusion. For SPIO-inclusion microbubbles, the maximum enhancement is observed at about 60 min and the enhancement starts to slowly disappear at 70 min after injection but does not completely return to the condition of pre-injection. According to the *in vitro* experiment, both the SPIO in the shell and the microbubbles themselves contribute to decrease the $T_2$ signal. When the SPIO-inclusion
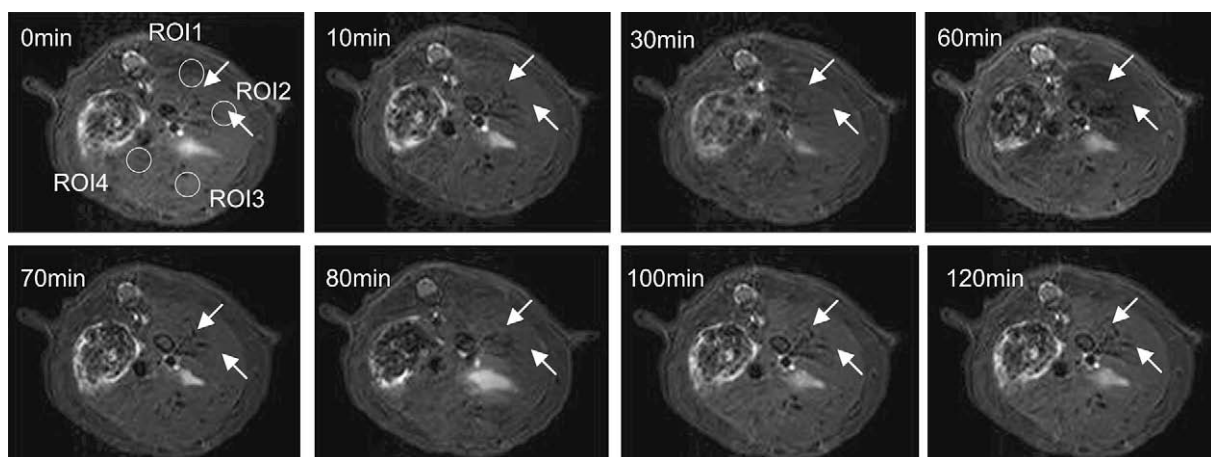


**Fig. 9.** Corresponding anatomical structure images from the same rat at two adjacent slice locations during SPIO-inclusion microbubble injection. The image shows that with the time lapse after injection, the $T_2$ signal in liver decreases at first and then increases (arrows). The first image shows the four ROIs to qualify the SNR.
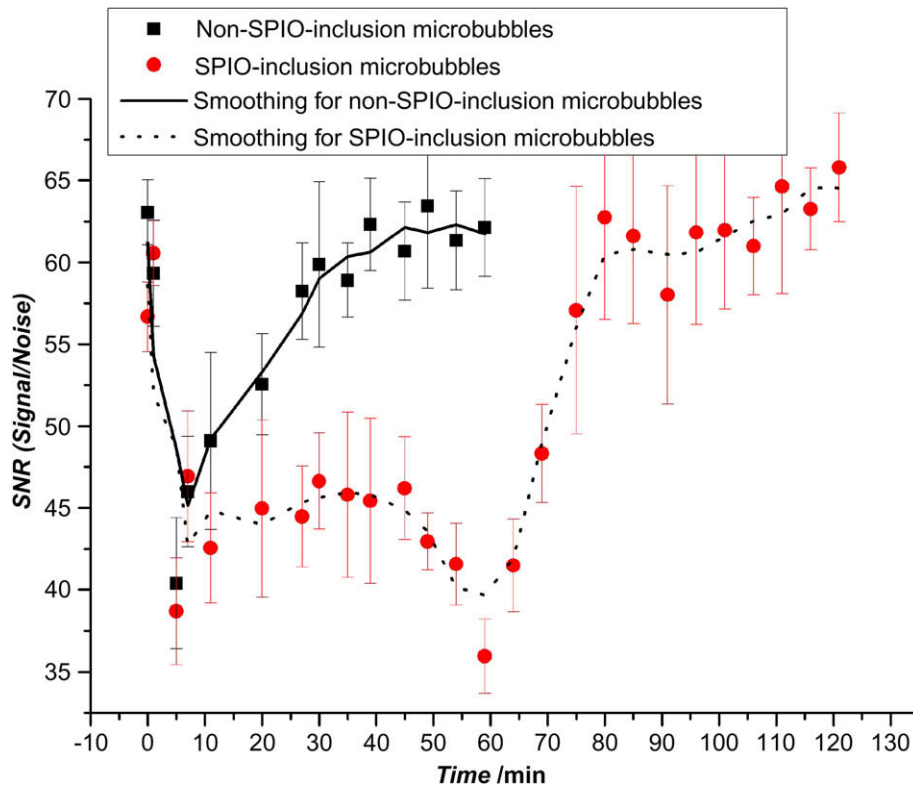
**Fig. 10.** The average SNR time-courses in four liver regions in the random rat experiment. The SNR time-course shows the different change tendencies after injection of non-SPIO-inclusion microbubbles and SPIO-inclusion microbubbles.

microbubbles enter into the blood vessels and tissues, the non-SPIO-inclusion microbubbles have shorter circulation cycle in rats because of their instability [32]. However, even if the SPIO-inclusion microbubbles are disrupted, the SPIO nanoparticles in the shell can be released, aggregated and accumulated in the liver tissue to further add the enhancement duration time.

### 3.7. The influence of shell susceptibility on MRI effect

The *in vitro* and *in vivo* MRI experiments all show that the microbubbles can be fabricated to be the effective MR susceptibility contrast agents. In our experiments, we examine the possibility of enhancing the effective magnetic susceptibility difference by embedding the different concentrations 12 nm $Fe_3O_4$ in the shell. The results show, although the shell components are biocompatible, which have relatively small magnetic permeabilities, the more concentration of SPIO in the shell will result in the stronger enhancement in the MRI. However, it is important to note that there is a strong dependence on the type of magnetically active agents, the nanoparticle radius, the magnetic saturation or total magnetic susceptibility, and the distribution in the shell. In general, large magnetic susceptibility [1] comes from SPIO particles.

### 4. Conclusion

In this study, we have produced and demonstrated that EMBs with the PLA and PVA double-layered polymer shell of 50–70 nm thicknesses can let the 12 nm SPIO $Fe_3O_4$ particles be loaded heterogeneously in their shell to significantly enhance magnetic susceptibility. The *in vitro* and *in vivo* MR susceptibility experiments demonstrate that it is possible that the microbubble susceptibility

effect can be significantly enhanced through the optimization of SPIO nanoparticles in the shell. At the meantime the resultant EMB can still maintain adequate echogenicity to be US contrast agents and keeping them acoustically active to participate sonoporation under moderate US exposure. Thus, the SPIO-inclusion microbubble can be manipulated instantaneously and locally *in vivo via* cavitation by the moderate US irradiation, which it might be possible to monitor *in vivo* contrast changes with the use of dynamic MR susceptibility imaging. Although this study mainly focused on the liver application, it can also be used for MR studies of other organs and tissues. The further application of these SPIO nanoparticle-embedded EMBs is that they can potentially be US and MRI dual contrast agents clinically.

### Appendix

Figures with essential colour discrimination. Figures 1, 3, 4, 10 of this article may be difficult to interpret in black and white. The full colour image can be found in the on-line version, at doi:10.1016/j.biomaterials.2009.03.051.

# References

[1] Yan GP, Robinson L, Hogg P. Magnetic resonance imaging contrast agents: overview and perspectives. Radiography 2007;13:e5–19.

[2] Schenck JF. The role of magnetic susceptibility in magnetic resonance imaging: MRI magnetic compatibility of the first and second kinds. Med Phys 1996;23(6):815–50.

[3] Quaia E. Microbubble ultrasound contrast agent: an update. Eur Radiol 2007;17:1995–2008.

[4] Cosgrove D. Ultrasound contrast agents: an overview. Eur J Radiol 2006;60:324–30.

[5] Wu JR, Nyborg WL. Ultrasound, cavitation bubbles and their interaction with cells. Adv Drug Deliv Rev 2008;60:1103–16.

[6] Ward M, Wu J, Chiu JF. Experimental study of the effects of Optison concentration on sonoporation in vitro. Ultrasound Med Biol 2000;26:1169–75.

[7] Wong KK, Huang I, Kim YR, Tang H, Yang ES, Kwong KK. In vivo study of microbubbles as an MR susceptibility contrast agent. Magn Reson Med 2004;52:445–52.

[8] Alexander AL, McCreery TT, Barrette TR, Gmitro AF, Unger EC. Microbubbles as novel pressure-sensitive MR contrast agents. Magn Reson Med 1996;35:801–6.

[9] Ueguchi T, Tanaka Y, Hamada S, Kawamoto R, Ogata Y, Matsumoto M, et al. Air microbubbles as MR susceptibility contrast agent at 1.5 Tesla. Magn Reson Med Sci 2006;5(3):147–50.

[10] Fain SB, Korosec FR, Holmes JH, O'Halloran R, Sorkness RL, Grist TM. Functional lung imaging using hyperpolarized gas MRI. J Magn Reson Imaging 2007;25:910–23.

[11] Dharmakumar R, Plewes DB, Wright GA. A novel microbubble construct for intracardiac or intravascular MR manometry: a theoretical study. Phys Med Biol 2005;50:4745–62.

[12] Dharmakumar R, Plewes DB, Wright GA. On the parameters affecting the sensitivity of MR measures of pressure with microbubbles. Magn Reson Med 2002;47:264–73.

[13] Binder WH, Sachsenhofer R, Farnik D, Blaas D. Guiding the location of nanoparticles into vesicular structures: a morphological study. Phys Chem Chem Phys 2007;9:6435–41.

[14] Wan J, Cai W, Meng X, Liu E. Monodisperse water-soluble magnetite nanoparticles prepared by polyol process for high-performance magnetic resonance images. Chem Commun 2007:5004–6.

[15] Gupta AK, Cupta M. Synthesis and surface engineering of iron oxide nanoparticles for biomedical applications. Biomaterials 2005;26:3995–4021.

[16] Correas JM, Bridal L, Lesavre A, Mejean A, Helenon MCO. Ultrasound contrast agents: properties, principles of action, tolerance, and artifacts. Eur Radiol 2001;11:1316–28.

[17] Raisinghani A, DeMaria AD. Physical principle of microbubble ultrasound contrast agents. Am J Cardiol 2002;190(Suppl):3J–7J.

[18] Sun C, Lee JSH, Zhang MQ. Magnetic nanoparticles in MR imaging and drug delivery. Adv Drug Deliv Rev 2008;60(11):1252–65.

[19] Borden MA, Zhang H, Gillies RJ, Dayton PA, Ferrara KW. A stimulus-responsive contrast agent for ultrasound molecular imaging. Biomaterials 2008;29:597–606.

[20] Tartis MS, Kruse DE, Zheng HR, Zhang H, Kheirolomoom A, Marik J, et al. Dynamic microPET imaging of ultrasound contrast agents and lipid delivery. J Control Release 2008;131(3):160–6.

[21] Cai WB, Chen XY. Nanoplatforms for targeted molecular imaging in living subjects. Small 2007;3(11):1840–54.

[22] Endoh M, Koibuchi N, Sato M, Morishita R, Kanzaki T, Murata Y, et al. Fetal gene transfer by intrauterine injection with microbubbleenhanced ultrasound. Mol Ther 2002;5:501–8.

[23] Lu QL, Liang HD, Partridge T, Blomley MJ. Microbubble ultrasound improves the efficiency of gene transduction in skeletal muscle in vivo with reduced tissue damage. Gene Ther 2003;10:396–405.

[24] Yang F, Li L, Li Y, Chen Z, Wu JR, Gu N. Superparamagnetic nanoparticle-inclusion microbubbles for ultrasound contrast agents. Phys Med Biol 2008;53:6129–41.

[25] Pisani E, Tsapis N, Paris J, Nicolas V, Cattel L, Fattal E. Polymeric nano/micro-capsules of liquid perfluorocarbons for ultrasonic imaging: physical characterization. Langmuir 2006;22:4397–402.

[26] Paradossi G, Cavalieri F, Chiessi E, Ponassi V, Martorana V. Tailoring of Physical and chemical properties of macro- and microhydrogels based on Telechelic PVA. Biomacromolecules 2002;3:1255–62.

[27] Chen Z, Zhang Y, Zhang S, Xia J, Liu J, Xu K, et al. Preparation and characterization of water-soluble monodisperse magnetic iron oxide nanoparticles via surface double-exchange with DMSA. Colloid Surface A 2008;316:210–6.

[28] Liu X, Kaminski MD, Chen H, Torno M, Taylor LA, Rosengart J. Synthesis and characterization of highly-magnetic biodegradable poly (D,L-lactide-co-glycolide) nanospheres. J Control Release 2007;119:52–8.

[29] Feshitana JA, Chena CC, Kwana JJ, Borden MA. Microbubble size isolation by differential centrifugation. J Colloid Interface Sci 2009;329(2):316–24.

[30] Hong RY, Feng B, Chen LL, Liu GH, Li HZ, Zheng Y, et al. Synthesis, characterization and MRI application of dextran-coated $Fe_3O_4$ magnetic nanoparticles. Biochem Eng J 2008;42(3):290–300.

[31] Xi XY, Yang F, Chen D, Luo Y, Zhang D, Gu N, et al. A targeting drug-delivery model via interactions among cells and liposomes under ultrasonic excitation. Phys Med Biol 2008;53:3251–65.

[32] Wu J, Tong J. Experimental study of stability of a contrast agent in an ultrasound field. Ultrasound Med Biol 1998;24(2):257–65.